Journal of Advanced Ceramics
先进陶瓷
ISSN 2226-4108
CN 10-1154/TQ
清华大学出版社 Tsinghua University Press
SciOpen

J Adv Ceram 2026, **15**: 9221408

https://doi.org/10.26599/JAC.2026.9221408

Research Article

Solvation structure induced solvent-mediated growth of Li_2O_2 and uniform deposition of Li^+ for high-performance lithium-oxygen batteries

Daming Yang[1], Guiru Sun[1,2,*], Sheng Wang[1,3], Siwen Deng[1], Lei Huang[1], Ze Gao[1], Jiajun Wang[1], Tong Wu[4], Wei Lu[1,3], Ming Feng[1,2,*]

[1]*Key Laboratory of Functional Materials Physics and Chemistry of the Ministry of Education, School of Chemistry, Jilin Normal University, Changchun 130103, China.*

[2]*Changbaishan Laboratory, Jilin University, Changchun 130012, China.*

[3]*College of Information Technology, Jilin Engineering Research Center of Optoelectronic Materials and Devices, Jilin Normal University, Siping 136000, China*

[4]*College of Chemistry and Materials Science, Inner Mongolia Minzu University, Tongliao 028000, China.*

* Corresponding author.

E-mail: G. Sun, sungr@jlnu.edu.cn;

M. Feng, mingfeng@jlnu.edu.cn

Received: September 30, 2026; Revised: November 6, 2026; Accepted: November 14, 2026

©The Author(s) 2026

Just Accepted

Abstract: The practical application of Li-O_2 batteries is limited by sluggish oxygen redox kinetics and dendritic Li growth. Here, we introduce 6-bromoxoindole (6-Br-Oxind) as a multifunctional electrolyte additive to regulate Li^+ solvation, guide solution-mediated Li_2O_2 growth, and stabilize Li plating. After partial deprotonation, 6-Br-Oxind coordinates with Li^+ to form 6-Br-Oxind···Li^+ species that capture soluble O_2^-/LiO_2 intermediates and promote their conversion into Li_2O_2 through a solution-mediated pathway. The same solvation structure weakens Li^+-TEGDME coordination, lowers the Li^+ desolvation barrier, and establishes a more uniform Li^+ flux at the anode. Meanwhile, Br^- released from 6-Br-Oxind and F^- generated from $TFSI^-$ decomposition form a LiBr@LiF-rich solid electrolyte interphase that further suppresses dendritic Li deposition. As a result, Li-O_2 batteries with 6-Br-Oxind show enhanced reversibility, a low overpotential of 0.81 V, and extended cycling stability, while Li||Li symmetric cells operate stably for 1,300 h. This work demonstrates a solvation-structure strategy for coupling cathode reaction regulation with anode interphase stabilization in Li-O_2 batteries.

Keywords: Li-O_2 batteries; 6-bromoxoindole; solvation structure; solvent-mediated pathway; SEI film

1 Introduction

Rechargeable Lithium-oxygen (Li-O_2) batteries are promising energy-storage systems because their theoretical energy density (~3500 Wh kg^{-1}) is far higher than that of conventional Li-ion batteries.[1–5] Their operation relies on the reversible formation and decomposition of Li_2O_2 ($2Li^+ + O_2 + 2e^- \leftrightarrow Li_2O_2$, $E^0 = 2.96$ V).[6] During discharge, O_2 is reduced at the cathode to O_2^-, which then associates with Li^+ to form LiO_2. Li_2O_2 can subsequently grow through either a surface-mediated or a solution-mediated pathway, depending on the electron-donating ability of the electrolyte solvent.[7,8] In the surface-mediated route, Li_2O_2 forms as an insulating film on the cathode, causing cathode passivation,

Just Accepted

high overpotential, and limited discharge capacity.[9,10] By contrast, solution-mediated LiO_2 diffusion promotes toroidal Li_2O_2 deposition in the electrolyte and markedly improves capacity.[11] Precise control over the Li_2O_2 growth pathway is therefore central to mitigating cathode passivation and improving Li-O_2 battery performance.

At present, most regulations of the solution mediated growth pathway of Li_2O_2 rely primarily on electrolytes with high donor numbers (DNs) (e.g., DMSO and DMF) along with minor soluble redox mediators (RMs) (e.g., H_2O, AQ, and ABTS).[12–16] However, molecules in high donor number electrolytes typically undergo redox reactions with highly reactive lithium metal to form organolithium compounds and generate a large number of side reactions.[12,17] In addition, the shuttle effect of RMs can severely corrode the Li anode, leading to the formation of a large amount of dead lithium and rapid capacity fading of the Li-O_2 battery. Furthermore, proton/high acceptor-number species such as H_2O can promote solution-mediated Li_2O_2 growth by hydrogen-bonding to O_2^-/LiO_2, but excess uncoordinated protons tend to form LiOH/Li_2O and corrode the Li anode. [18–20] Designing and incorporating appropriate soluble additives into low DN electrolytes (e.g., TEGDME) to regulate the solvation structure of the electrolyte represents an effective strategy for modulating the solution mediated growth of Li_2O_2, as well as an efficient pathway to promote uniform Li^+ deposition. Recently, solvation-structure regulation has emerged as a promising strategy for aprotic Li-O_2 batteries: nitrile additives can induce the formation of sheet-like Li_2O_2 and stabilize the Li anode,[21] ether cosolvents can trigger an anionic solvation transition that enables reversible Li anodes at low temperatures.[22] Nevertheless, soluble additives that simultaneously steer solution-mediated Li_2O_2 growth at the cathode and homogenize Li^+ deposition at the anode through a rationally designed solvation structure remain rarely explored. Among numerous additives, indole and its derivatives are favored due to advantages such as low cost, rich electronic structures, and the possibility of functionalization at multiple adsorption sites.[23] Indole is typically a benzopyrrole containing a pyrrole ring. Its unique -NH group tends to undergo single-electron reactions, resulting in the substitution of H by Li^+ and the

Just Accepted

combination with the N site to form an organic salt, which accelerates the rapid transfer of Li^+.[24] Zhou et al. introduced 6-bromoxoindole (6-Br-Oxind) into lithium-sulfur (Li-S) batteries and achieved rapid Li^+ transfer and uniform Li^+ deposition through the solvation structure of 6-Br-Oxind···Li^+ formed after 6-Br-Oxind deprotonation with Li^+.[25]

In Li-O_2 batteries, the 6-Br-Oxind···Li^+ solvation structure features a positively polarized Li^+ center, which could electrostatically interact with negatively charged O_2^-. This interaction is a typical Coulombic interaction (Coulomb attraction), which originates from the electrostatic force between oppositely charged species. As a result, the Li^+ center in the 6-Br-Oxind···Li^+ could effectively attract and stabilize soluble LiO_2 intermediates in the electrolyte. The stabilized LiO_2 species can subsequently diffuse into the bulk electrolyte and undergo further reduction or disproportionation reactions to form Li_2O_2, thereby promoting a solution-mediated Li_2O_2 growth pathway. Furthermore, the formation of solvation structures may also facilitate the Li^+ deposition behavior on the anode. Ma et al. demonstrated that the dynamic coordination process within the solvation structure can lower the desolvation energy barrier for Li^+ at the interface, which enhances the interfacial reduction kinetics of anions and suppresses the side reactions of electrolyte solvent molecules at the anode sides.[26] In this context, the preferential coordination between 6-Br-Oxind and Li^+ could be expected to weaken the strong interaction between Li^+ and solvent molecules (TEGDME), thereby lowering the Li^+ desolvation energy barrier. The resultant faster desolvation kinetics may help mitigate local Li^+ concentration polarization, which can produce a more uniform ionic flux distribution and potentially allow highly homogeneous Li deposition. Additionally, the C-Br bond of 6-Br-Oxind is cleaved during cycling, and the released Br^- reacts with Li^+ to form a robust LiBr SEI film on the surface of the Li anode, further inhibiting the growth of Li dendrites.[25]

Here, we design a 6-Br-Oxind-containing TEGDME electrolyte to couple solution-mediated Li_2O_2 growth at the cathode with uniform Li^+ deposition at the anode. 6-Br-Oxind partially deprotonates in the electrolyte and forms 6-Br-Oxind···Li^+ solvation structures. At the cathode, these species interact

Just Accepted

with O_2^- to form 6-Br-Oxind···LiO_2 intermediates, promoting solution-mediated Li_2O_2 formation. At the anode, preferential 6-Br-Oxind-Li^+ coordination weakens Li^+-TEGDME binding, facilitates Li^+ desolvation, and homogenizes Li^+ flux. Meanwhile, Br^- released from 6-Br-Oxind and F^- derived from $TFSI^-$ decomposition jointly form a LiBr@LiF-rich SEI. The synergy between optimized solvation kinetics and a robust interphase enables stable Li plating/stripping. As a result, Li-O_2 batteries with 6-Br-Oxind deliver a low overpotential of 0.81 V, improved rate performance, and extended cycling stability. Li||Li symmetric cells with 6-Br-Oxind also sustain 1,300 h of cycling, compared with 300 h for cells without 6-Br-Oxind. These findings expand the molecular design space for electrolyte additives in Li-O_2 batteries.

2 Experimental

2.1 Preparation of electrolytes

LiTFSI (Sigma-Aldrich, 99.9%) and 6-Br-Oxind (Aladdin Reagent, 98%) were dried under vacuum at 70 °C for 24 h before use. Tetraethylene glycol dimethyl ether (TEGDME, Aladdin Reagent, ≥99.7%) was dried with activated 3 Å molecular sieves (Sigma-Aldrich) to remove residual water. A 1 M LiTFSI/TEGDME electrolyte was prepared as the baseline electrolyte. The 6-Br-Oxind-containing electrolyte was prepared by dissolving 6-Br-Oxind in 1 M LiTFSI/TEGDME at a mass ratio of 1%, 2%, and 3%.

2.2 Electrochemical measurements

Galvanostatic discharge/charge tests of Li-O_2 and Li||Li symmetric batteries were performed on a NEWARE battery testing system (CT-4008T, Shenzhen Neware Electronics Co., Ltd.) in an O_2-filled glovebox (H_2O < 0.5 ppm). CV measurements under different atmospheres were carried out on an electrochemical workstation (Solartron 1470E, AMETEK) using a three-electrode configuration with a glassy carbon working electrode, a Pt counter electrode, and a $LiFePO_4$ reference electrode. The potential window was -1.5 to 1.2 V vs. $LiFePO_4$, and the scan rate was 10 mV s^{-1}. LSV tests were conducted on the same workstation from 3.0 to 2.4 V and from 3.0 to 4.5 V at 1 mV s^{-1}. EIS

Just Accepted

measurements were also performed on the Solartron 1470E over a frequency range of 10^{-2} to 10^{5} Hz. O_2 consumption and O_2/CO_2 evolution during discharge/charge were monitored by DEMS (PrismaPro, Pfeiffer Vacuum).

2.3 Characterization

The morphologies of cathodes and anodes were observed by SEM (S-5500, Hitachi) and TEM (Talos F200X G2, Thermo Fisher Scientific). FTIR spectra of electrolytes from Li-O_2 batteries at different discharge/charge states were recorded on a Nicolet 6700 spectrometer (Thermo Fisher Scientific). The phase evolution of cathodes during cycling was characterized by in situ XRD (D/Max 2500, Rigaku). XPS (ESZALB 250XL) was used to analyse the elemental composition and chemical states of cycled Li anodes. O_2^- signals in different electrolytes were tracked with an EPR spectrometer (JESFA200, JEOL). NMR measurements of electrolytes with and without 6-Br-Oxind were performed on a Bruker AVANCE 400 spectrometer.

3 Results and Discussion

Molecular dynamics (MD) simulation using the model in Fig. S1 are employed to investigate the effect of 6-Br-Oxind addition on the electrolyte. **Fig. 1**a, 1b, S2a and S2b present representative snapshots from the MD simulations of the electrolyte with 6-Br-Oxind and without 6-Br-Oxind at 0 ns and 50 ns. Compared with the representative snapshot of the electrolyte at 0 ns, the Li^+ in the electrolytes (both with and without 6-Br-Oxind) exhibit a dispersed distribution with a large number of Li^+ in aggregation around the anions, forming a coordination structure with the anions. The radial distribution functions (RDFs) and coordination numbers of Li^+ with other ions and solvent molecules in electrolytes with and without 6-Br-Oxind are calculated (Fig. 1c and S2c). The RDF is the important function for describing the structural characteristics of fluids, which is defined as shown in Eq. (1), where ρ_β is the number density of β particles, and $N_{\alpha\beta}(r)$ represents the average number of β particles within a sphere centered at an α particle with a radius of r.

Just Accepted

$$g_{\alpha\beta}(r)=\frac{1}{4\pi\rho_{\beta}r^2}\left[\frac{dN_{\alpha\beta}(r)}{dr}\right] \quad (1)$$

In the electrolyte without 6-Br-Oxind, the RDF peak between Li^+ and O atoms of $TFSI^-$ is observed at 1.94 Å with a coordination number of 0.737, whereas the peak for Li^+ and O atoms of TEGDME appears at 1.88 Å, showing a coordination number of 5.221. For the electrolyte with 6-Br-Oxind, the RDF peak for Li^+ and O of $TFSI^-$ shifts to 1.92 Å, accompanied by an increased coordination number of 0.750 (Fig. S2c). In contrast, although the RDF peak position for Li^+ and O of TEGDME remains at 1.88 Å, its coordination number declines to 4.955. These changes indicate that 6-Br-Oxind promotes Li^+ coordination with $TFSI^-$ while weakening its interaction with TEGDME. Furthermore, distinct RDF peaks are detected for Li^+ with atoms in 6-Br-$Oxind^-$: at 1.86 Å for O (coordination number 0.109) and at 2.02 Å for N (coordination number 0.048) (Fig. 1c). These results clearly demonstrate the formation of a 6-Br-Oxind$\cdots Li^+$ solvation structure. Finally, the distribution of various solvation structures during the simulation is statistically analyzed. As shown in Fig. S3, the most dominant solvation structure in both the 6-Br-Oxind-free and 6-Br-Oxind-containing electrolytes is Li(1)TFSI(1)TEGDME(1). However, in the electrolyte with 6-Br-Oxind, multiple Li-6-Br-Oxind solvation structures are observed. Note that among the top three most prevalent structures in this system, two involve Li-TFSI coordination modes-one more than in the electrolyte without 6-Br-Oxind (Fig. S4). This structural evolution indicates that 6-Br-$Oxind^-$ can directly coordinate with Li^+ to form stable solvation complexes (Fig. 1d). By competing with TEGDME for coordination sites, 6-Br-$Oxind^-$ effectively reduces the proportion of TEGDME in the primary solvation shell of Li^+, further demonstrating the role of 6-Br-Oxind additive in modulating the Li^+ solvation environment.

Just Accepted

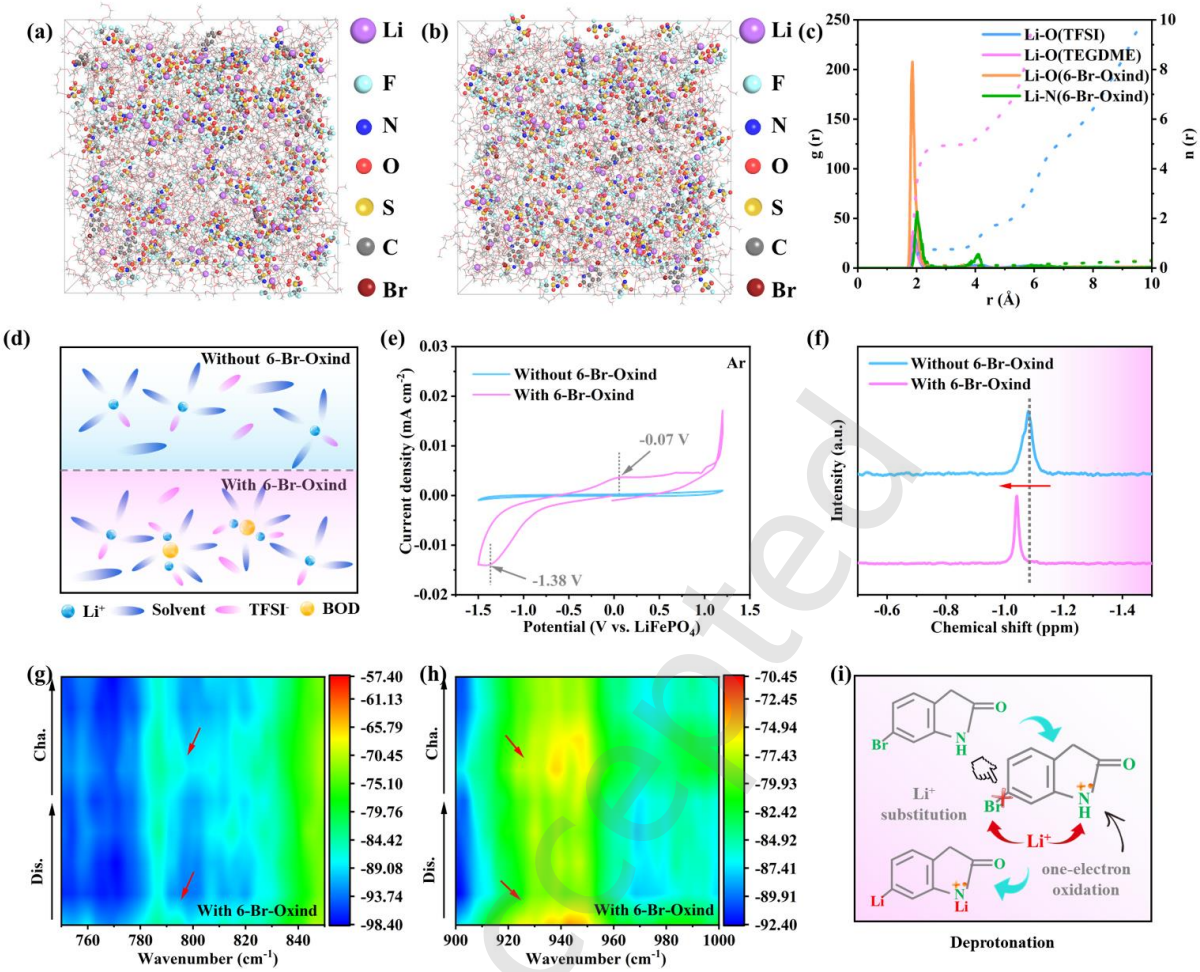


Fig. 1 Snapshots of the MD simulations at (a) 0 and (b) 50 ns for the electrolytes with 6-Br-Oxind. (c) RDF curves and coordination numbers of electrolytes with 6-Br-Oxind. (d) Schematic illustrations of Li^+ solvation structures of the electrolyte with 6-Br-Oxind. (e) CV curves of Li-O_2 batteries with and without 6-Br-Oxind at a scan rate of 10 mV s^{-1} under an Ar atmosphere with a voltage range of -1.5~1.2 V vs. $LiFePO_4$. (f) The ^7Li NMR spectra of the electrolyte with and without 6-Br-Oxind. (g, h) Locally magnified 2D mapping images corresponding to the ex-situ FTIR spectra of the electrolyte in the Li-O_2 batteries with 6-Br-Oxind in different discharge/charge states. (i) Deprotonation of 6-Br-Oxind and recombination process with Li^+.

To determine the optimal content of 6-Br-Oxind, cyclic voltammetry (CV) curves of the Li-O_2 batteries assembled with electrolytes containing different additive concentrations (1%, 2%, and 3 wt%) were collected, as shown in Fig. S5. The CV curve of the battery with 2 wt% 6-Br-Oxind exhibits the higher ORR and OER current densities than those of the batteries with 1 wt% and 3 wt% 6-Br-Oxind,

Just Accepted

and thus 2 wt% was adopted for the subsequent experiments. To investigate the electrochemical behavior of 6-Br-Oxind in the electrolyte, CV analysis is systematically performed on a model Li-O_2 battery with and without 6-Br-Oxind in the electrolyte under controlled Ar and O_2 atmospheres, with a voltage range of -1.5~1.2 V vs. $LiFePO_4$ at a scan rate of 10 mV s^{-1}.As shown in Fig. 1e, there is no peak in the CV curve for the battery without 6-Br-Oxind in the Ar atmosphere, indicating that no redox reaction occurred during cycling. For the battery with 6-Br-Oxind, two distinct peaks appear at -1.38 V and -0.07 V in the CV curve. These peaks correspond to the oxidation and reduction processes of 6-Br-Oxind, specifically attributed to its deprotonation and reprotonation.[27,28] In the O_2 atmosphere, apart from the peaks related to 6-Br-Oxind's deprotonation/reprotonation, the battery with 6-Br-Oxind exhibits reduction and oxidation peaks at -0.85 V and 1.01 V, corresponding to the ORR and OER processes, respectively. In contrast, the reduction peak (-0.96 V) and oxidation peak (1.03 V) of the battery without 6-Br-Oxind are higher and lower than those of the battery with 6-Br-Oxind (Fig. S6), respectively, indicating that 6-Br-Oxind can effectively promote charge transfer kinetics and optimize interfacial electron transport mechanisms. Subsequently, ^{7}Li nuclear magnetic resonance (^{7}Li NMR) spectra are used to further investigate the coordination environment of Li^+ in the electrolyte, as shown in Fig. 1f. The chemical shift of the peak in the spectrum of the electrolyte without 6-Br-Oxind is -1.08 ppm, which is significantly lower than that (-1.04 ppm) of the electrolyte with 6-Br-Oxind. This difference indicates a reduction in electron density around the Li^+, resulting in a deshielding effect on the Li^+ nucleus. This observation suggests that upon deprotonation, 6-Br-Oxind coordinates with Li^+ to form the 6-Br-Oxind$\cdots Li^+$ solvation structure.[29] As shown in Fig. S7a and S8, ex-situ fourier transform infrared (FTIR) spectra is used to detect the changes in the functional groups of the electrolyte of the battery without and with 6-Br-Oxind after discharged and charged for 10 to 40 h at 100 mA h g^{-1}. The characteristic signals of TEGDME and $TFSI^-$ are detected in the electrolyte without 6-Br-Oxind (Fig. S7a-c). In Fig. S7a, for the TEGDME, the peak at 1187 cm^{-1} is regarded as -CH_3, while the ether linkage demonstrates tripartite absorption features at 849, 1057, and 1135 cm^{-1},

Just Accepted

corresponding to C-O-C asymmetric stretching modes.[30] For the $TFSI^-$, the peak at 1024 cm^{-1} arises from symmetric S-N-S bending vibrations, whereas the peak at 1335 cm^{-1} originates from sulfonyl group S=O=S stretching. Notes that there is almost no shift of all peaks during the discharge and charge processes (Fig. S7b and S7c). In the electrolyte with 6-Br-Oxind, apart from the peaks of $-CH_3$, C-O-C, S-N-S, and S=O=S, peaks are observed at 679 cm^{-1} and 794/928 cm^{-1}, corresponding to the out-of-plane bending vibrations of C-Br and benzene ring C-H groups of 6-Br-Oxind (Fig. S8), respectively.[25] The intensity variations of C-Br stretching (679 cm^{-1}) and C-H bending modes (794/928 cm^{-1}) further demonstrate that 6-Br-Oxind undergoes sequential deprotonation accompanied by multi-site coordination with Li^+ to form a 6-Br-Oxind···Li^+ solvation structure during the discharge and charge processes (Fig. 1g and 1h).[31,32] Fig. 1i illustrates the process of 6-Br-Oxind undergoing deprotonation in the electrolyte and subsequently forming a 6-Br-Oxind···Li^+ solvation structure with Li^+. 6-Br-Oxind undergoes partial deprotonation and binds with Li^+ and anions in the electrolyte to stabilize its structure during discharging and charging. This behavior stems from the tendency of the p-π conjugation cyclic amide groups to dehydrogenate in Li salt-containing organic electrolytes, forming stable Li-N bonds that modulate Li^+ transport.[25,33–35] In addition, no obvious peak was detected before ~4 V in the LSV curve of the battery assembled with the 6-Br-Oxind electrolyte, indicating that 6-Br-Oxind does not attack the electrolyte and thus avoids unnecessary decomposition and side reactions (Fig. S9).

To verify the impact of the 6-Br-Oxind···Li^+ solvation structure on Li^+ diffusion, CV curves of the Li-O_2 batteries with and without 6-Br-Oxind are obtained at various scan rates (5~100 mV s^{-1}) within a potential range of 2.2~4.5 V, as shown in Fig. S10a-d. The distinct oxidation peaks are observed at 3.38 V and 3.26 V during the OER process in the CV curves at a scan rate of 5 mV s^{-1} for batteries without and with 6-Br-Oxind (Fig. S10a and S10b), respectively, which are attributed to the decomposition of Li_2O_2. Note that the peaks associated with Li_2O_2 decomposition exhibit a positive shift (toward high voltages) with increasing scan rate, which is attributed to insufficient time to

Just Accepted

surmount the kinetic barrier, resulting in a reduction in reaction kinetics (Fig. S10c and S10d). Furthermore, the Randles-Sevcik plots show the Li^+ diffusion coefficient (D_{Li^+}) in the batteries with and without 6-Br-Oxind, as shown in Fig. S11a and S11b. The D_{Li^+} of the battery with 6-Br-Oxind is 3.47×10^{-11} cm^2 s^{-1}, which is significantly higher than that (1.56×10^{-11} cm^2 s^{-1}) of the battery without 6-Br-Oxind, suggesting the enhancement Li^+ diffusivity after adding 6-Br-Oxind, which results from the 6-Br-Oxind···Li^+ solvation structure. To further explore the effect of 6-Br-Oxind on Li^+ diffusion in the battery, galvanostatic intermittent titration technique (GITT) curves are recorded for batteries without and with 6-Br-Oxind. The average D_{Li^+} of batteries without 6-Br-Oxind during the charge-discharge process is 1.929×10^{-11} cm^2 s^{-1} (Fig. S12). In contrast, the D_{Li^+} of batteries with 6-Br-Oxind is increased by ~3 times (5.578×10^{-11} cm^2 s^{-1}) (**Fig. 2**a), which is consistent with the test results of CV at different scan rates. Fig. S13 show the impedance of steel||steel symmetric batteries with and without 6-Br-Oxind at different temperatures. The impedance values of the battery without 6-Br-Oxind at 25, 35, 45, 55, and 65 °C are 2.057, 1.973, 1.854, 1.615, and 1.480 Ω (Fig. S13a), respectively, significantly higher than those (1.879, 1.810, 1.665, 1.497, and 1.403 Ω) of the battery with 6-Br-Oxind (Fig. S13b). Furthermore, ionic conductivities (σ_i) at different temperatures are calculated from the impedance values of the battery, as shown in Fig. S14. Similarly, at different temperatures, the σ_i of electrolytes with 6-Br-Oxind are consistently higher than those of electrolytes without 6-Br-Oxind, suggesting that 6-Br-Oxind···Li^+ interactions may reduce the stability of Li^+ solvation shells, rendering Li^+ easily dissociable from the shells and thus accelerating ionic migration. Activation energies (E_a) of electrolytes with and without 6-Br-Oxind are calculated via the Arrhenius equation, as shown in Fig. 2b. The E_a of the electrolyte with 6-Br-Oxind is 0.094 eV, which is lower than that (0.101 eV) of the electrolyte without 6-Br-Oxind, indicating a small energy barrier for ionic migration in the electrolyte with 6-Br-Oxind. In Fig. 2c and S15, the electronic conductivity (σ_e) of the electrolyte with and without 6-Br-Oxind are obtained by the constant voltage polarization method. The σ_e of the electrolytes with and without 6-Br-Oxind are 3.22×10^{-10} and 3.64×10^{-10} S cm^{-1}, respectively. A low σ_e corresponds to

Just Accepted

the ability to inhibit the growth of lithium dendrites inside the electrolyte.[36]

The O_2^- signal in various electrolytes containing KO_2 are detected using electron paramagnetic resonance (EPR) spectroscopy, as shown in Fig. 2d. The fluctuations are observed at ~325 mT in the spectra of crown ether (CE)+KO_2, LiTFSI+CE+KO_2, and 6-Br-Oxind+CE+KO_2 electrolytes, which are considered to be the signals of O_2^-, indicating that 6-Br-Oxind does not interact with O_2^-. Notably, no O_2^- signal is detected in the 6-Br-Oxind+LiTFSI+CE+KO_2 electrolyte, possibly due to the interaction between the generated 6-Br-Oxind$\cdots Li^+$ solvation structure and O_2^- in the electrolyte, indicating that 6-Br-Oxind$\cdots Li^+$ can capture O_2^- and alter the pathway of O_2^- disproportionation to accelerate the disproportionation rate, thereby promoting the kinetics of the discharge and charge processes. To further confirm the interaction between the 6-Br-Oxind$\cdots Li^+$ solvation structure and O_2^-, in situ UV-vis absorption spectroscopy was performed on the electrolyte containing 6-Br-Oxind during discharge and charge, as shown in Fig. S16. The characteristic absorption peak of 6-Br-Oxind at 252 nm is clearly observed, and its intensity varies during the discharge and charge processes. This variation is attributed to the interaction between the 6-Br-Oxind$\cdots Li^+$ solvation structure and O_2^-, further confirming that the 6-Br-Oxind$\cdots Li^+$ species interacts with and stabilizes soluble superoxide/LiO_2 intermediates in the electrolyte.

Just Accepted

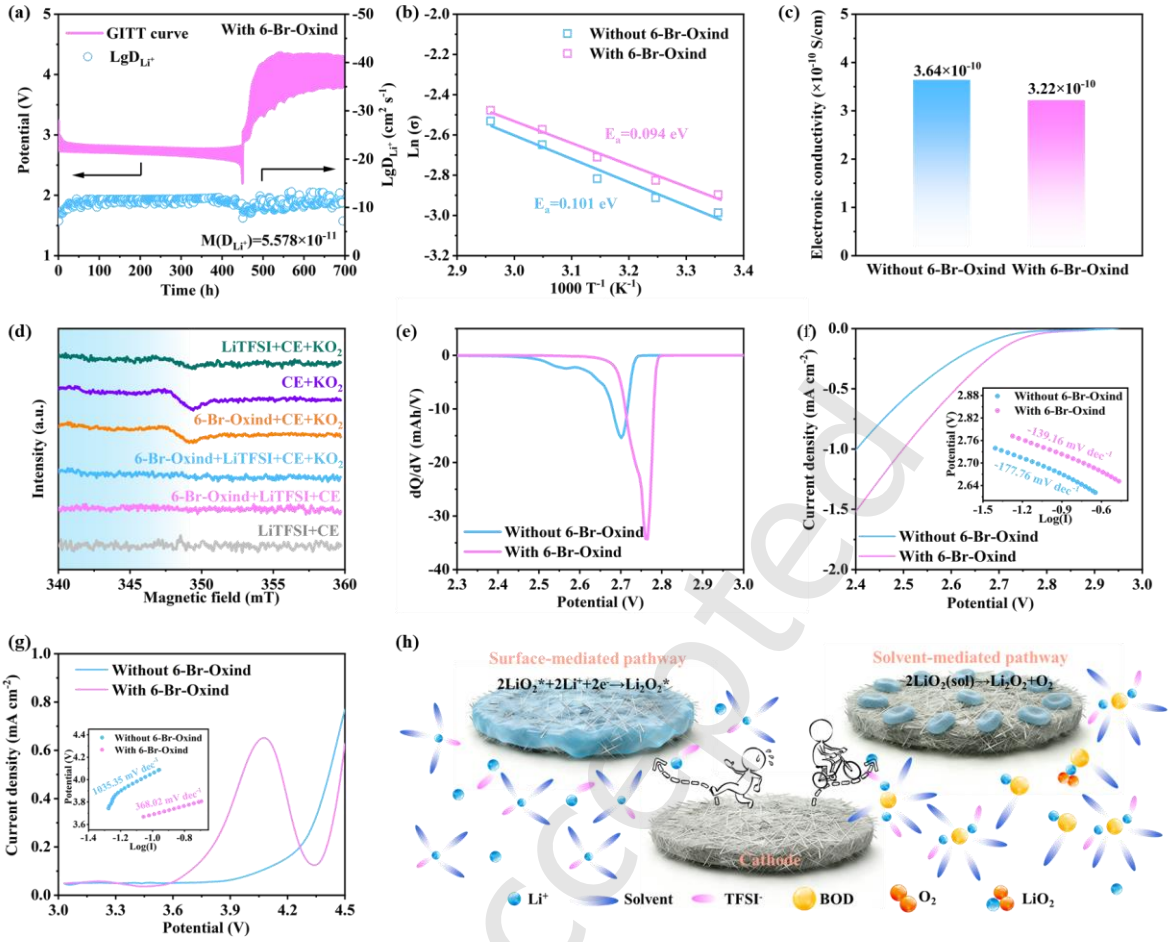


Fig. 2 (a) GITT curve of the batteries with 6-Br-Oxind. (b) Arrhenius curve of the σ_i and (c) σ_e of electrolytes with and without 6-Br-Oxind. (d) EPR spectra of different electrolytes. (e) dQ/dV curves of the batteries with and without 6-Br-Oxind. The LSV curves of (f) ORR and (g) OER processes for the Li-O_2 batteries without and with 6-Br-Oxind; The insets correspond to the Tafel curves obtained by calculating from the LSV curves. (h) The discharge and charge mechanism diagrams of the Li-O_2 battery with 6-Br-Oxind.

To further verify the effect of 6-Br-Oxind on discharge products, differential capacity (dQ/dV) curves of batteries with and without 6-Br-Oxind are obtained, as shown in Fig. 2e. The dQ/dV curves of batteries with and without 6-Br-Oxind during discharge exhibit two peaks at ~2.76 V and ~2.70 V, respectively, indicating that 6-Br-Oxind promotes the formation of Li_2O_2. Notably, the area enclosed by the dQ/dV curve of the battery with 6-Br-Oxind and the x-axis is significantly larger than that of the battery without 6-Br-Oxind, indicating that 6-Br-Oxind can enhance the discharge capacity of the

Just Accepted

battery. To examine the influence of the 6-Br-Oxind on the ORR and OER processes of the battery, we obtain the linear sweep voltammetry (LSV) curves of the battery without and with 6-Br-Oxind. Fig. 2f is the LSV curves for the ORR process of the battery at a scan rate of 1 mV s^{-1} within a potential range of 3.0~2.4 V. The battery with 6-Br-Oxind exhibits higher current density and onset potential than that of the battery without 6-Br-Oxind, suggesting that the 6-Br-Oxind can facilitate ORR kinetics. The Tafel plots based on LSV are calculated as shown in the inset of Fig. 2f. The Tafel slope of the battery with 6-Br-Oxind is -139.16 mV dec^{-1}, which is significantly smaller than that (-177.76 mV dec^{-1}) of the battery without 6-Br-Oxind. Furthermore, the LSV curves of the OER process of the batteries without and with 6-Br-Oxind are collected by using cathodes containing Li_2O_2 (prepared from SP and commercial Li_2O_2) at a scan rate of 1 mV s^{-1} within the voltage range of 3.0~4.5 V. In Fig. 2g, the battery with 6-Br-Oxind reveals a higher current density and a lower onset voltage of the anode peak related to the decomposition of Li_2O_2 than that of the battery without 6-Br-Oxind. Similarly, the battery with 6-Br-Oxind exhibits a higher Tafel slope (368.02 mV dec^{-1}) compared to that (1,035.35 mV dec^{-1}) of the battery without 6-Br-Oxind, confirming the promoting effect of 6-Br-Oxind on the OER process (the inset of Fig. 2g).

Based on the above experiments, a solvation structure regulated discharge/charge mechanism for the Li-O_2 battery with 6-Br-Oxind is proposed, as illustrated in Fig. 2h. In the LiTFSI/TEGDME electrolyte, 6-Br-Oxind coordinates with Li^+ and partially reconstructs the original Li^+ solvation sheath, forming 6-Br-Oxind···Li^+ species with modified Li^+ solvation environments. During discharge, dissolved O_2 is reduced at the cathode to generate O_2^-. The pre-existing 6-Br-Oxind···Li^+ species readily interact with O_2^- to form a transient 6-Br-Oxind···LiO_2 intermediate, which stabilizes the highly reactive LiO_2 and promotes its dissolution/diffusion in the electrolyte. As a result, Li_2O_2 preferentially forms through a solution-mediated growth pathway rather than direct surface deposition, leading to enlarged Li_2O_2 particles and improved discharge capacity. During charging, Li_2O_2 is oxidatively decomposed, releasing Li^+ back into the electrolyte. The regenerated 6-Br-Oxind

Just Accepted

molecules rapidly recapture Li^+ to reform 6-Br-Oxind···Li^+, thereby maintaining the optimized Li^+ solvation structure. This dynamic coordination accelerates Li^+ migration away from the cathode, alleviates local Li^+ accumulation and concentration polarization, and lowers the energy barrier for Li_2O_2 decomposition. Meanwhile, the regulated Li^+ solvation/desolvation behavior also contributes to more uniform Li^+ deposition on the lithium anode. Therefore, 6-Br-Oxind-induced solvation structure regulation simultaneously promotes solvent-mediated Li_2O_2 growth at the cathode and uniform Li^+ deposition at the anode, accounting for the enhanced electrochemical performance of the Li-O_2 battery.

The morphologies of the discharge products of the Li-O_2 batteries with and without 6-Br-Oxind are studied by scanning electron microscopy (SEM) at a current density of 200 mA g^{-1}. Fig. S17 shows the SEM image of the battery cathode, which reveals that SP particles are uniformly distributed on the surface of CP. In **Fig. 3**a, a film-like discharge products are formed on the cathode of the battery without 6-Br-Oxind after discharge, which results in a serious blockage of the cathode pores and a hindrance to the diffusion of O_2, leading to the premature termination of the discharge reaction.[37] In contrast, ring-shaped discharge products are formed on the cathode of the battery with 6-Br-Oxind after discharge (Fig. 3b). The ring-shaped Li_2O_2 is ~0.25 μm in size and creates a porous and loose structure (Fig. S18), promoting the transmission of O_2 and increasing the discharge capacity. To identify the discharge products, in-situ X-ray diffraction (XRD) is used to monitor the cathodes of the Li-O_2 batteries with and without 6-Br-Oxind. In Fig. 3c and 3d, diffraction peaks emerge at 32.90° and 35.00° during the discharge process and gradually intensify, exhibiting good agreement with the standard pattern of Li_2O_2 (PDF No. 09-0355), indicating that the discharge products of both the batteries without 6-Br-Oxind and with 6-Br-Oxind are Li_2O_2. During the charge, the diffraction peaks intensity of Li_2O_2 gradually decreases until it completely disappears, and no new peaks emerge, demonstrating that both the batteries without and with 6-Br-Oxind exhibit good reversibility during the first cycle. Note that the full width at half maximum (FWHM) of the peaks for the battery with 6-Br-Oxind is 0.389 and 0.558, which is significantly lower than that (0.470 and 0.589) of the battery

Just Accepted

without 6-Br-Oxind (Fig. 3e), indicating that the crystallinity of Li_2O_2 formed in the battery with 6-Br-Oxind is increased, which is consistent with the SEM results.

The reversibility of the batteries with and without 6-Br-Oxind is further investigated using differential electrochemical mass spectrometry (DEMS) to characterize the gas consumption and formation during the cycling process in Fig. 3f and 3g. During the discharge process, both the batteries with and without 6-Br-Oxind consume O_2, with O_2 generation occurring during the charge process. The e^-/O_2 values of the Li-O_2 batteries are calculated by measuring the area under the O_2 evolution curve and comparing it with the number of electron transfers. The calculated e^-/O_2 values are 1.81 and 1.89 for the batteries without and with 6-Br-Oxind, respectively, which are close to the theoretical value of 2, confirming a typical two-electron transfer process (Fig. S19). Note that the battery without 6-Br-Oxind generates CO_2 towards the end of charging, which is attributed to the decomposition of the electrolyte under high potential.[38] In contrast, the CO_2 evolution curve of the battery with 6-Br-Oxind remains unchanged, further confirming the good stability of the battery with 6-Br-Oxind [39]. Moreover, the SEM images of cathodes for the batteries with and without 6-Br-Oxind after 40 cycles are obtained, as shown in Fig. S20a and S20b. In Fig. S20a, an indecomposable film-like product is formed on the cathode surface of the battery without 6-Br-Oxind after 40 cycles. In contrast, under the same conditions, the cathode surface of the battery with 6-Br-Oxind remains free of newly formed substances (Fig. S20b). The FTIR spectra of those cathodes are obtained to confirm the indecomposable film-like product. In Fig. 3h, the spectrum of the cathode in the battery without 6-Br-Oxind can be observed to closely resemble the standard Li_2CO_3 spectrum, indicating that the film-like product on the cathode is Li_2CO_3.[40] This is attributed to the side reaction in which CO_2 generated from the decomposition of the electrolyte under high voltage combines with Li^+, which is consistent with the DEMS results. These results demonstrate that the addition of 6-Br-Oxind effectively suppresses the side reactions of the battery, thereby significantly enhancing the cyclic stability of the battery.

Just Accepted

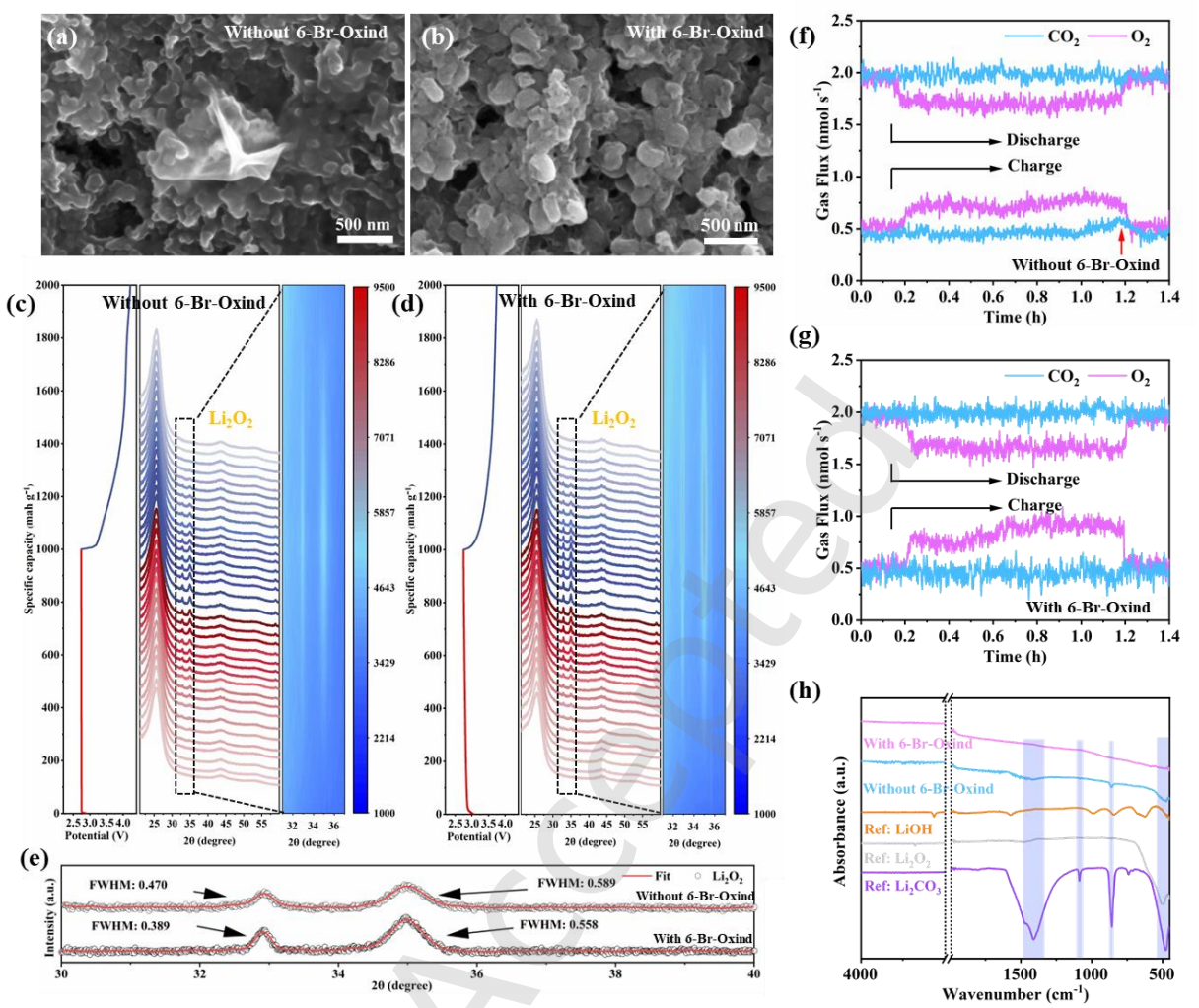


Fig. 3 SEM images of cathodes in the Li-O_2 batteries (a) without and (b) with 6-Br-Oxind after the 1st discharge. In-situ XRD patterns of cathodes in the Li-O_2 batteries (c) without and (d) with 6-Br-Oxind, (e) corresponding enlarged partial image. Real-time concentrations of O_2 and CO_2 during discharge and charge processes of the batteries (f) without and (g) with 6-Br-Oxind. (h) FTIR spectra of cathodes from batteries with and without 6-Br-Oxind cycled for 40 cycles.

To investigate the impact of the 6-Br-Oxind···Li^+ solvation structure on the flux of Li^+ at the anode interface, the morphological evolution of the Li anode in the Li-O_2 batteries with and without 6-Br-Oxind is examined using SEM for different numbers of cycles at a current density of 250 mA g^{-1}. Fig. S21 shows the initially smooth and flat Li foil. In batteries without the 6-Br-Oxind, initial corrosion and pore formation are observed on the Li anode after 10 cycles (Fig. S22a). The number of pores exhibits a significant increase after 20 cycles, as shown in Fig. S22b. Ultimately, after 40 cycles, a

Just Accepted

substantial amount of Li dendrites and dead Li forms on the Li anode (**Fig. 4**a), which is likely attributed to parasitic reactions between the Li anode and the electrolyte. For batteries with 6-Br-Oxind, the Li anode remains smooth and intact after 10 and 20 cycles (Fig. S22c and S22d). Notably, the Li anode surface remains flat and free of dendrites even after 40 cycles (Fig. 4b). This is attributed to the 6-Br-Oxind···Li^+ solvation structure weakening the Li^+-TEGDME interaction, reducing the desolvation energy barrier, which is consistent with the MD simulations results.

To confirm the surface composition of the Li anode, X-ray photoelectron spectroscopy (XPS) spectra of the Li anode in Li-O_2 batteries with and without 6-Br-Oxind after 40 cycles are obtained, as shown in Fig. S23, 4c, and 4d. In Fig. S23, the Li 1s spectrum of the battery with 6-Br-Oxind exhibits three distinct peaks, corresponding to LiBr (56.8 eV), Li_2O (55.9 eV), and LiF (55.3 eV), while only Li_2O and LiF are observed in the battery without 6-Br-Oxind. Similarly, in the Br 3d spectra, two peaks are assigned to C_xH_yBr (69.6 eV) and LiBr (68.6 eV) for the battery with 6-Br-Oxind, whereas no Br signal is detected in spectrum of the battery without 6-Br-Oxind (Fig. 4c). The formation of LiBr is attributed to the in situ reaction between Br^- from 6-Br-Oxind dissociation and the Li anode. In Fig. 4d, the F 1s spectrum reveals two peaks attributed to CF_3 (688.9 eV) and LiF (684.8 eV). These results indicate that the formed SEI film consists of LiBr and LiF, termed a LiBr@LiF-rich SEI film. The 6-Br-Oxind···Li^+ solvation structure and the LiBr@LiF-rich SEI film act synergistically as a barrier against Li dendrite formation and to mitigate parasitic reactions among the Li anode, electrolyte, and O_2. Additionally, high-resolution transmission electron microscopy (HR-TEM) images of the cycled LiBr@LiF-rich SEI film are obtained, as shown in Fig. 4e. In Fig. 4e, a distinct lamellar structure of the SEI film is clearly observable. Fig. 4f and 4g present the lattice fringes corresponding to the region in Fig. 4e. These images exhibit lattice spacings of 3.17 Å and 2.33 Å, corresponding to the (111) crystalline planes of LiBr and LiF, respectively.[41] It is reported that the (111) crystal facets of LiBr and LiF exhibit low adsorption energy and low Li^+ diffusion barriers, which facilitate the adsorption and rapid diffusion of Li^+. These results demonstrate that the LiBr@LiF-rich SEI film can accelerate

Just Accepted

Li^+ diffusion and inhibit Li dendrite growth, thereby improving battery lifespan, which is consistent with the experimental findings.

The Li^+ transference number (t_{Li^+}) is inversely correlated with Li dendrite growth kinetics according to Sand's time equation (S1): as t_{Li^+} approaches 1, dendritic propagation is significantly suppressed.[42] Notably, the calculated t_{Li^+} values for the 6-Br-Oxind-free and 6-Br-Oxind-containing electrolytes are determined as 0.640 and 0.729, respectively, which demonstrates that the 6-Br-Oxind···Li^+ configuration facilitates accelerated Li^+ migration, thereby contributing to dendrite inhibition as shown in Fig. S24a and S24b.

To further explore the influence of the 6-Br-Oxind on the interfacial stability of the Li anode, the CV curves of Li||Li symmetric batteries without and with 6-Br-Oxind are collected at a scan rate of 50 mV s^{-1} with a potential range of -0.3~0.3 V vs. Li/Li^+. During the cycling, the current density of the battery without 6-Br-Oxind gradually decreases (Fig. S25). In contrast, the current density of the battery with 6-Br-Oxind maintains good stability, indicating that the 6-Br-Oxind is beneficial to improving the plating/stripping stability of the Li||Li symmetric battery with 6-Br-Oxind (Fig. 4h). Furthermore, the exchange current density (I_0) is calculated to evaluate the electrode kinetics as shown in Fig. 4i. The I_0 of the battery with 6-Br-Oxind is 0.717 mA cm^{-2}, which is significantly higher than that (0.201 mA cm^{-2}) of the battery without 6-Br-Oxind, proving that 6-Br-Oxind improves the electrochemical kinetics of the battery. Similarly, the redox characteristics of Li||Cu batteries with and without 6-Br-Oxind are investigated by CV at a scan rate of 0.1 mV s^{-1} within the range of -0.25~1.5 V. In Fig. S26, a pair of redox peaks correspond to the plating and stripping of Li. Note that the peak current density of the battery with 6-Br-Oxind is higher than that without 6-Br-Oxind, further confirming the enhancement of the 6-Br-Oxind···Li^+ solvation structure on the plating/stripping kinetics of the battery. Fig. 4j and S27 demonstrate the galvanostatic discharge/charge curves of Li||Li symmetric batteries with and without 6-Br-Oxind at a current density of 0.2 mA cm^{-2}, within a capacity limit of 0.2 mAh cm^{-2}. In Fig. 4j, the battery without 6-Br-Oxind exhibits a sharp voltage increase after

Just Accepted

300 h of cycling, which results from the severe parasitic reactions and the accumulation of dead Li. In contrast, the battery with 6-Br-Oxind stably cycles for 1,300 h (Fig. 4j and S22). Note that the battery with 6-Br-Oxind displays a higher initial overpotential than that without 6-Br-Oxind within the first 100 h, resulting from the synergistic contribution of Br^- released from 6-Br-Oxind and F^- dissociated from $TFSI^-$ to form a stable SEI film on the Li anode.

To elucidate the pivotal roles of 6-Br-Oxind···Li^+ solvation structure and the LiBr@LiF-rich SEI film in facilitating Li deposition, the in-situ optical microscopy tests are conducted on Li||Li symmetric batteries with and without 6-Br-Oxind under a current density of 2 mA cm^{-2} with continuous discharging for 1 h. For batteries without 6-Br-Oxind, the Li anode progressively develops continuous mossy dendrites accompanied by severe Li swelling with increasing time (Fig. 4k). In contrast, a compact film forms on the Li anode surface alongside uniform Li deposition over time for batteries with 6-Br-Oxind (Fig. 4l). These results demonstrate that the 6-Br-Oxind···Li^+ solvation structure and LiBr@LiF-rich SEI film effectively enhances the stability of the anode/electrolyte interface. Fig. S28 presents the SEM images of Li anodes after 100, 200, and 300 cycles under a current density of 0.2 mA cm^{-2}. For the batteries without 6-Br-Oxind, the Li anode becomes uneven, with numerous pores after 100 cycles as shown in Fig. S28a. After 200 cycles, the Li anode develops increased porosity with emerging dendrites and dead Li (Fig. S28b). Subsequently, the anode surface exhibits a substantial deposition of fine dendrites alongside abundant granular dead Li after 300 cycles (Fig. S28c). For batteries with 6-Br-Oxind, a small number of granular products emerge on the Li anode after 100 cycles (Fig. S28d). Later, the particles gradually grow and coalesce into interconnected flattened structures (Fig. S28e). Ultimately, a smooth and uniform SEI film forms on the Li anode after 300 cycles (Fig. S28f). The XPS spectra of Li anode after 200 cycles further confirm that the SEI film is composed of both LiBr and LiF, originating from Br^- in 6-Br-Oxind and dissociated F^- in the electrolyte (Fig. S29a-c).

Just Accepted

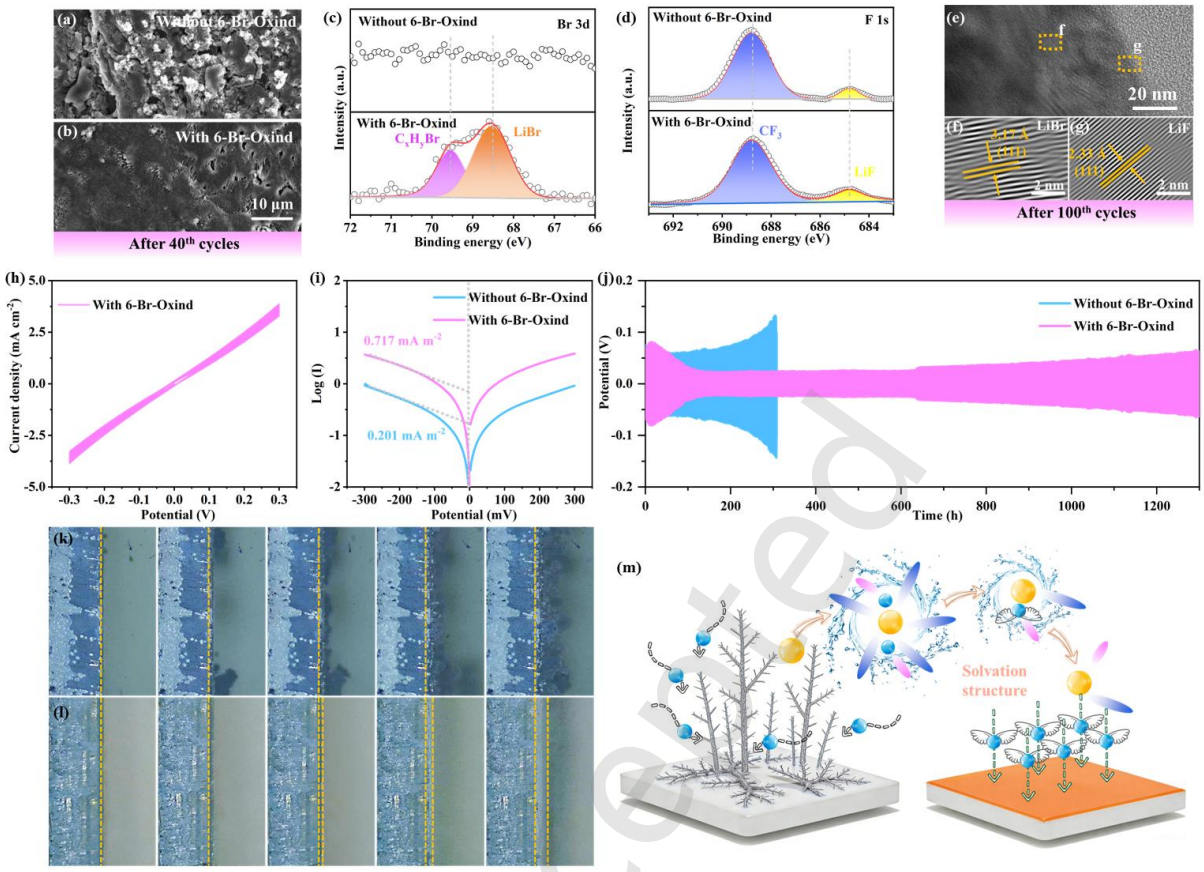


Fig. 4 SEM images of Li anodes in the Li-O_2 batteries (a) without and (b) with 6-Br-Oxind after 40 cycles. XPS spectra of (c) Br 3d and (d) F 1s for the Li-O_2 batteries with and without 6-Br-Oxind after 40 cycles. (e) HR-TEM images of the Li anode cycled 100th with 6-Br-Oxind. (f, g) Magnified image of the boxed area in Fig. 4e. (h) CV curve of the Li||Li symmetric battery with 6-Br-Oxind at a scan rate of 50 mV s^{-1}. (i) Tafel plots of the Li||Li symmetric battery with and without 6-Br-Oxind. (j) Voltage hysteresis of Li plating/stripping with and without 6-Br-Oxind. In-situ optical microscopy of Li deposition process (k) without and (l) with 6-Br-Oxind at a current density of 2 mA cm^{-2}. (m) Schematic diagram of Li deposition for the Li-O_2 batteries without and with 6-Br-Oxind.

Based on the experimental findings, a protective mechanism of the 6-Br-Oxind-containing electrolyte for Li anode is proposed. In Fig. 4m, non-uniform charge distribution on the Li anode during cycling leads to heterogeneous Li^+ deposition in the battery without 6-Br-Oxind, resulting in rampant dendrite growth and dead Li formation. In contrast, for the battery with 6-Br-Oxind, the deprotonated 6-Br-Oxind forms a stable 6-Br-Oxind···Li^+ solvation structure, which competes with

Just Accepted

the solvent TEGDME for coordination sites, significantly reducing the coordination number of Li^+ with TEGDME, while simultaneously enhancing the participation of $TFSI^-$ anions in the Li^+ coordination environment. Subsequently, the Br^- released from 6-Br-Oxind and the F^- generated from the $TFSI^-$ at the anode interface react in situ with Li^+ to form a LiBr@LiF-rich SEI film, which provides fast transport channels for Li^+ migration and promotes horizontal dispersion of Li^+ flux. The synergistic effect of the 6-Br-Oxind···Li^+ solvation structure and LiBr@LiF-rich SEI film effectively suppress Li dendritic growth and stabilizes the electrode-electrolyte interface.

Fig. 5a presents the first galvanostatic current discharge curves of Li-O_2 batteries with and without 6-Br-Oxind at 250 mA g^{-1} with a cutoff potential of 2.2 V. The discharge capacity of the battery with 6-Br-Oxind increased by 136.54% compared with that of the battery without 6-Br-Oxind (from 4,677 mAh g^{-1} to 11,063 mAh g^{-1}). The first discharge-charge curves of the batteries with and without 6-Br-Oxind are obtained at 100 mA g^{-1} within a cut-off capacity of 500 mAh g^{-1}, as shown in Fig. 5b. It can be clearly observed that the overpotential of the battery is reduced from 1.09 V to 0.81 V by the addition of 6-Br-Oxind, corresponding to the round-trip efficiency increasing from 71.61% to 77.43%. To further exclude the potential contribution of Br^- to the ORR and OER kinetics, the initial discharge/charge profiles of cells employing electrolytes with different additives were examined (Fig. S30). Notably, the cell containing N-methylated 6-Br-Oxind and alkaline proton scavengers exhibited no appreciable reduction in overpotential, indicating that Br^- makes a negligible contribution to the enhanced reaction kinetics in this system. In contrast, a pronounced decrease in overpotential was observed for the cell employing Br-free oxindole, further suggesting that the improved ORR/OER kinetics primarily originate from the specific coordination structure formed between 6-Br-Oxind···Li^+, rather than from Br^- itself. The rate performance of the batteries without and with 6-Br-Oxind at current densities of 100, 250, and 500 mA g^{-1} is evaluated, as shown in Fig. 5c and 5d. In Fig. 5c, the overpotentials of the battery without 6-Br-Oxind are 1.09, 1.28, and 1.57 V at 100, 250, and 500 mA g^{-1}, respectively. The rapid increase in overpotential might be caused by the limited Li^+ transport

Just Accepted

kinetics.[43] In contrast, the battery with 6-Br-Oxind shows excellent rate performance, in which the overpotential are 0.81, 0.89, and 0.95 V at 100, 250, and 500 mA g^{-1} (Fig. 5d), further demonstrating the promoting effect of 6-Br-Oxind···Li^+ on Li^+ conduction. Furthermore, the recyclability of the batteries with and without 6-Br-Oxind at different current densities (100, 250, and 500 mA g^{-1}) is evaluated within a cut-off capacity of 500 mAh g^{-1}. In Fig. 5e and S31a, the battery without 6-Br-Oxind only exhibits 67 cycles at 100 mA g^{-1}. In contrast, the battery with 6-Br-Oxind shows good cycling stability, which can maintain 468 cycles under the same test conditions (Fig. 5e and S31b). Additionally, the battery with 6-Br-Oxind remains more stable at 250 mA g^{-1} and 500 mA g^{-1}, maintaining 175 and 150 cycles, respectively, than those (45 and 24 cycles) of the battery without 6-Br-Oxind (Fig. S32 and S33). In addition, FTIR spectra of the electrolytes collected from the Li-O_2 batteries with 6-Br-Oxind after different numbers of cycles were recorded, as shown in Fig. S34. Two characteristic absorption bands are observed at 1,617 and 1,712 cm^{-1}, corresponding to the aromatic C=C and lactam C=O stretching vibrations of 6-Br-Oxind, respectively. Notably, with increasing cycle numbers, these bands neither disappear nor shift, confirming that the skeletal structure of 6-Br-Oxind in the electrolyte remains stable.

Just Accepted

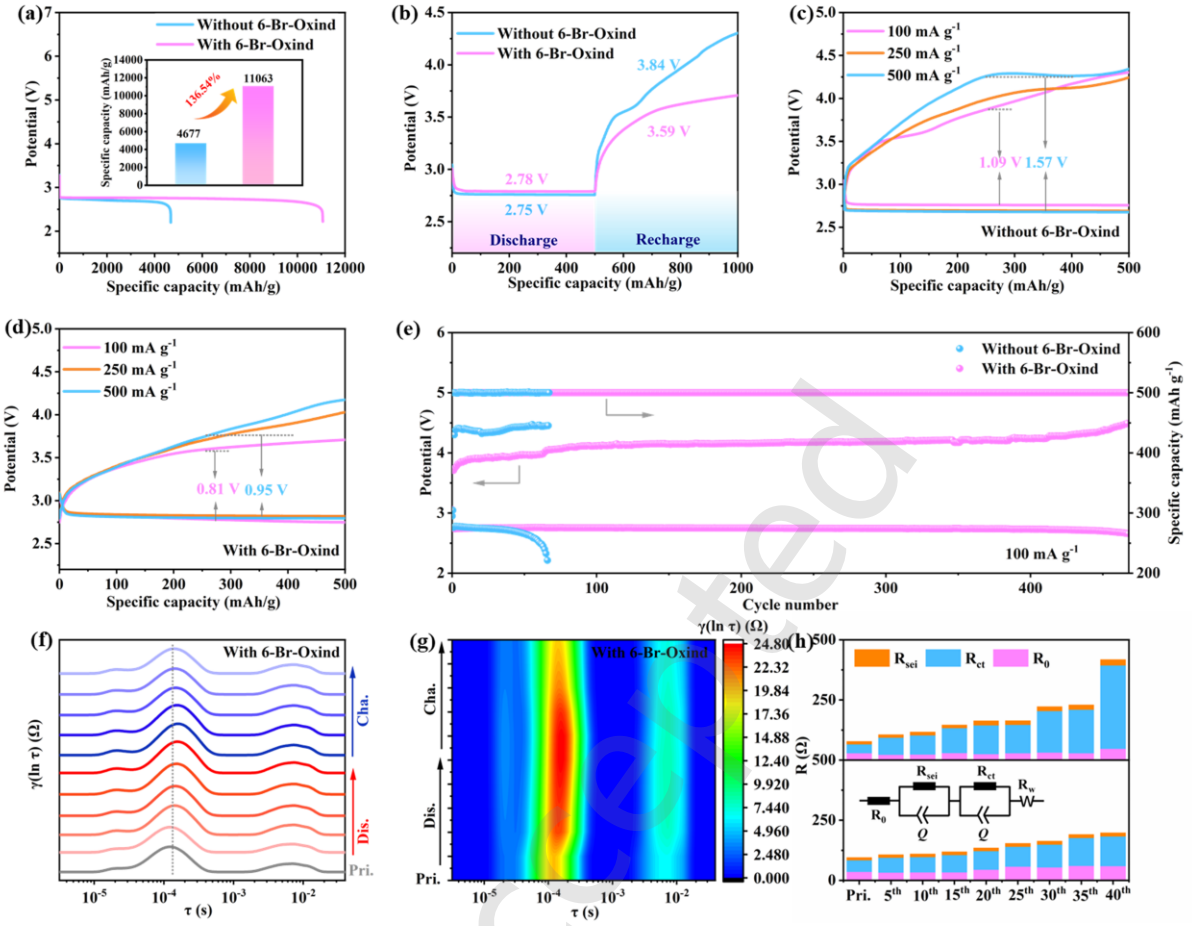


Fig. 5 (a) Discharge curves and (b) first discharge and recharge curves of batteries with and without 6-Br-Oxind. First discharge and charge curves of batteries (c) without and (d) with 6-Br-Oxind at various current density. (e) Corresponding cycle number associated with terminal discharge/charge voltage and delivered discharge. (f) DRT images corresponding to in-situ EIS and (g) contour plot of corresponding DRT of the battery with 6-Br-Oxind. (h) Fitted R_0, R_{sei}, and R_{ct} values of the batteries with and without 6-Br-Oxind at different cycle numbers. The inset shows the equivalent circuit corresponding to the Nyquist plots.

Highly insulating Li_2O_2 accumulates at the cathode during discharge, leading to an increase in battery resistance and even battery failure. Here, the changes in internal resistance of batteries with and without 6-Br-Oxind during discharge and charge processes are monitored by in-situ electrochemical impedance spectroscopy (EIS), at a current density of 100 mA g^{-1}. Fig. S35a and S35b show the Nyquist plots of batteries without and with 6-Br-Oxind, which are monitored every 10 min

Just Accepted

during 50 min of discharge and charge processes. The distribution of relaxation times (DRT) is used to decompose the high-frequency region of the in-situ EIS to identify the dominant chemical reactions occurring within the battery. Within the range of 10^{-6} to 10^{-1} s, three peaks with time constants τ_1 = ~10^{-5}, τ_2 = ~10^{-4}, and τ_3 = ~10^{-2}, are considered to be three different electrochemical processes, corresponding to contact resistance, the resistance of Li^+ passing through the SEI film, and the resistance of Li_2O_2 formation and decomposition, respectively (Fig. 5f, 5g, S36a, and S36b).[44, 45] In Fig. 5f and 5g, the peak at τ_2 shifts toward low frequencies during discharge, indicating increased resistance to Li^+ migration on the anode, which could be caused by the roughening of the Li anode surface due to Li^+ stripping. During charging, the peak at τ_2 shifts toward high frequencies, suggesting an enhancement Li^+ migration rate on the anode, which can be attributed to the formation of SEI film that facilitates rapid Li^+ transfer. The peak at τ_3 increases during discharging and decreases to the same value as the initial impedance during charging, which demonstrates the good reversibility of the battery with 6-Br-Oxind. In contrast, for the battery without 6-Br-Oxind, the peak at τ_2 shifts continuously toward lower frequencies during both discharge and charge processes, indicating the hindrance of the migration rate of Li^+ on the anode surface, which could be attributed to the uneven stripping and deposition of Li^+ during cycling, resulting in impaired Li^+ migration (Fig. S36a and S36b). Similarly, the peak at τ_3 does not decrease to the same value as the initial impedance after charging, suggesting that a trace amount of Li_2O_2 remains on the cathode of the battery without 6-Br-Oxind after charging. Notably, the relaxation times corresponding to the peaks at τ_2 and τ_3 for the battery with 6-Br-Oxind are significantly shorter than those for the battery without 6-Br-Oxind, indicating the enhancement of Li^+ migration rates and the improvement in the formation/decomposition kinetics of Li_2O_2 in the battery with 6-Br-Oxind (Fig. S37). The impedance of batteries with and without 6-Br-Oxind during 0 to 40 cycles was further analyzed by EIS, as shown in Fig. S38 and 5i. The Nyquist plots exhibit a semicircle and a diffusion part (Fig. S38a and S38b). According to the equivalent circuit shown in the inset of Fig 5h, these features correspond to ohmic resistance (R_0), SEI film resistance (R_{sei}), charge

Just Accepted

transfer resistance (R_{ct}), and diffusion resistance (R_w), respectively. In Fig. 5h, the R_t ($R_0 + R_{sei} + R_{ct}$) value of the battery without 6-Br-Oxind increase significantly from 78.42 Ω to 418.24 Ω during 0 to 40 cycles. In contrast, the battery with 6-Br-Oxind shows a slow increase in R_t value (from 95.50 Ω to 198.39 Ω) over the same cycle range, indicating enhanced reversibility of the battery with 6-Br-Oxind.

4 Conclusion

In summary, 6-Br-Oxind as a functional electrolyte additive in Li-O_2 batteries, effectively enhancing the ORR and OER kinetics and promoting anode interface stability. Specifically, during the discharge process, 6-Br-Oxind undergoes partial deprotonation and forms a 6-Br-Oxind···Li^+. The 6-Br-Oxind···Li^+ effectively captures and stabilizes O_2^- species via Coulombic interaction, thereby guiding the solution-mediated growth of Li_2O_2 and reducing the battery overpotential. Equally, the electron-rich π-conjugated structure of 6-Br-Oxind enables its participation in the primary solvation sheath of Li^+, weakening the strong interaction between Li^+ and TEGDME solvent molecules. This significantly reduces the desolvation energy barrier for Li^+, which not only optimizes Li^+ transport kinetics but also establishes a uniform Li^+ flux at the anode interface, guiding homogeneous Li deposition. Moreover, the Br^- component from 6-Br-Oxind molecules can be sacrificially released during cycling, interacting with F^- generated from $TFSI^-$ anion decomposition to form a robust composite LiBr@LiF-rich SEI film on the Li anode. This SEI film effectively suppresses Li dendrite growth, enhancing the cycling stability of the battery. Therefore, the Li-O_2 battery with 6-Br-Oxind exhibits a low overpotential of 0.81 V and a prolonged cycle life of 468 cycles. Furthermore, the Li||Li symmetric battery with 6-Br-Oxind demonstrates exceptional cycling stability of 1,300 h, compared with 300 h for the battery without 6-Br-Oxind. This work undoubtedly provides novel insights into the development and application of soluble catalysts for Li-O_2 battery systems.

Just Accepted

Funding

This research was funded by the Scientific and Technological Innovation Project of Changbaishan Laboratory, Jilin Province (Grant No. CBSCBS2025003-01), and the National Natural Science Foundation of China (Grant No. 52471229).

Author contributions

Daming Yang: investigation, data curation, formal analysis, writing–original draft. Guiru Sun: conceptualization, methodology, supervision, writing–review and editing. Sheng Wang: conceptualization, formal analysis, software, validation. Siwen Deng: investigation, data curation, validation. Lei Huang: investigation, methodology, data curation. Ze Gao: investigation, software, formal analysis. Jiajun Wang: investigation, validation, data curation. Tong Wu: methodology, software, validation. Wei Lu: conceptualization, methodology, supervision. Ming Feng: funding acquisition, conceptualization, supervision, writing–review and editing.

Availability of data and materials

The data that support the findings of this study are available from the corresponding author upon reasonable request.

Competing interests

The authors have no competing interests to declare that are relevant to the content of this article.

Electronic Supplementary Material: Supplementary material (Figs. S1–S38) is available in the online version of this article.

References

[1] Jin Z, Su B, Wu S, Jiang C, *et al*. Tribocatalytic recycling of lithium-ion batteries. *J Adv Ceram* 2025, **14**: 9221121.

Just Accepted

[2] Gunhee P, Dong Won J, Il-Seop J, *et al*. Investigation of the effects of heteroatom doping on von-Alpen-type NASICON electrolytes and its applications to solid-state sodium batteries. *J Adv Ceram* 2025, **14**: 9221138.

[3] Su PY, Zheng XZ, Li SA, *et al.* Rationally tuning the oxidation state of the open active sites in Co-based MOFs to enhance the kinetics of Li-O_2 batteries. *Rare Met* 2025, **44**: 4595–4608.

[4] Tian SL, Song LN, Chang LM, *et al.* A magnetic/thermal coupling assisted lithium-oxygen battery based on magnetic heating effect of single atom-Co/MoS_2 cathode. *Chin Chem Lett* 2025: 111349.

[5] Arif M, Li X, Fu Z, *et al.* Photo-assisted Li/Zn-air batteries and supercapacitors: material design, working mechanism and challenges. *Adv Powder Mater* 2025, **4**: 100316.

[6] Zhou Y, Hong G, Zhang W. Nanoengineering of Cathode Catalysts for Li-O_2 Batteries. *ACS Nano* 2024, **18**: 16489–16504.

[7] Gou Z, Yao Y, Geng X, *et al.* Dual Redox Mediators Assisted Hierarchically Porous Hollow Carbon Shell Cathode for Enhanced Performance Li-O_2 Battery. *Adv Energy Mater* 2024, **14**: 2304272.

[8] Aetukuri NB, McCloskey BD, García JM, *et al.* Solvating additives drive solution-mediated electrochemistry and enhance toroid growth in non-aqueous Li-O_2 batteries. *Nat Chem* 2015, **7**: 50–56.

[9] Lyu Z, Zhou Y, Dai W, *et al.* Recent advances in understanding of the mechanism and control of Li_2O_2 formation in aprotic Li-O_2 batteries. *Chem Soc Rev* 2017, **46**: 6046–6072.

[10] Zhang Z, Dou Y, Zhao Z, *et al.* Unlocking the Energy Capabilities of Aprotic Lithium-Oxygen Batteries by Anion-Specific Adsorption Induced Interfacial Remodeling. *Adv Funct Mater* 2026, **36**: 2515490.

[11] Batcho TP, Leverick G, Shao-Horn Y, *et al.* Modeling the Effect of Lithium Superoxide Solvation and Surface Reduction Kinetics on Discharge Capacity in Lithium-Oxygen Batteries. *J Phys Chem C* 2019, **123**: 14272–14282.

Just Accepted

[12] Li B, Kogina T, Yang Z, *et al.* Unveiling oxygen reaction mechanisms on single-layer graphene surface in DMSO-based electrolyte for lithium-oxygen batteries by in situ EC-AFM observations. *Electrochim Acta* 2025: 146901.

[13] Womble MD, Cascio S, Wagner MJ. Prevention of Electrolyte Degradation in Lithium-Oxygen Batteries Using Highly Concentrated Electrolytes. *Appl Sci* 2025, **15**: 10233.

[14] Wang Y, Zhang T, Hao L. Unraveling the contribution of water to the discharge capacity of Li-O_2 batteries from a modelling perspective. *Appl Energy* 2024, **372**: 123852.

[15] Yu J, Zhang Q, Zhao B, *et al.* Repurposing Visible-Light-Excited Ene-Reductases for Diastereo- and Enantioselective Lactones Synthesis. *Angew Chem Int Ed* 2024, **63**: 202402673.

[16] Sun Z, Lin X, Dou W, *et al.* Redox Mediator with the Function of Intramolecularly Disproportionating Superoxide Intermediate Enabled High-Performance Li-O_2 Batteries. *Adv Energy Mater* 2022, **12**: 2102764.

[17] Togasaki N, Momma T, Osaka T. Enhanced cycling performance of a Li metal anode in a dimethylsulfoxide-based electrolyte using highly concentrated lithium salt for a lithium-oxygen battery. *J Power Sources* 2016, **307**: 98–104.

[18] Liao Y, Zhang X, Huang Z, *et al.* A Redox Mediator Containing Reversible Dynamic Boron-Oxygen Bonds to Construct an Adaptive SEI Layer for Advanced Li-O_2 Batteries. *ACS Appl Mater Interfaces* 2025, **17**: 19629–19637.

[19] Huang Z, Zhuang X, Li T, *et al.* $SnBr_2$ as a self-defense redox mediator enhances the cycle stability in lithium-oxygen batteries. *J Electroanal Chem* 2025: 119526.

[20] Wang QY, Zheng MT, Gao ML, *et al.* Simultaneously Generating Redox Mediator and Hybrid SEI for Lithium-oxygen Batteries by Lewis Acid Catalyzed Ring-opening Reaction of Organic Iodine. *Adv Funct Mater* 2024, **34**: 2312723.

[21] Li Z, Yu Y, Yang D, *et al*. A bifunctional nitrile additive for high-performance lithium-oxygen batteries. *Nano Res* 2024, 17: 6119-6126.

Just Accepted

[22] Huang Y, Fang H, Geng J, *et al*. Anionic Solvation Transition at Low Temperatures for Reversible Anodes in Lithium-Oxygen Batteries. *J Am Chem Soc* 2024, 146: 26516-26524.

[23] Ren KF, Du YF, Guo JX, *et al.* Multi-anion electrolyte modulates the interactions in solvation structure to construct robust lithium metal batteries. *J Energy Chem* 2025, **104**: 3643.

[24] Drăgoi CM, Nicolae AC, Dumitrescu IB. The Indole Scaffold in Biochemistry and Therapeutics: A Privileged Structure with Diverse Chemical, Biological, and Clinical Significance. *Targets* 2026, **4**: 4.

[25] Zou J, He P, Zhang Y, *et al.* An electrolyte additive of bromoxoindole enables uniform Li-ion flux and tunable Li_2S deposition for high-performance lithium–sulfur batteries. *J Mater Chem A* 2024, **12**: 5520–5529.

[26] Li Q, Liu G, Chen Y, *et al.* Electrolyte Solvent-Ion Configuration Deciphering Lithium Plating/Stripping Chemistry for High-Performance Lithium Metal Battery. *Adv Funct Mater* 2025, **35**: 2420327.

[27] Wang Y, Zhao XJ, Wu X, *et al.* Electrochemical Synthesis of Trisubstituted Oxazoles and Imines from β-Diketones and Amines. *ChemElectroChem* 2022, **9**: 202200378.

[28] Sun W, Zhou C, Fan Y, *et al.* Ion Co-storage in Porous Organic Frameworks through On-site Coulomb Interactions for High Energy and Power Density Batteries. *Angew Chem Int Ed* 2023, **62**: 202300158.

[29] Yao N, Chen X, Sun S, *et al.* Identifying the lithium bond and lithium ionic bond in electrolytes. *Chem* 2025, **11**: 102254.

[30] de Zea Bermudez V, Lucazeau G, Abello L, *et al.* Infrared and Raman spectroscopic study of polyether solutions of sulphamide Part I: Tetraethyleneglycol dimethyl ether and water. *J Mol Struct* 1993, **301**: 7–19.

[31] Olana BN, Lin SD, Hwang BJ. In situ diffuse reflectance infrared Fourier-transformed spectroscopy study of solid electrolyte interphase formation from lithium

Just Accepted

bis(trifluoromethanesulfonyl)imide in 1,2-dimethoxyethane and 1,3-dioxolane with and without lithium nitrate additive over lithium and copper metal anodes. *Electrochim Acta* 2022, **416**: 140266.

[32] Yu J, Lin X, Liu J, *et al.* In Situ Fabricated Quasi-Solid Polymer Electrolyte for High-Energy-Density Lithium Metal Battery Capable of Subzero Operation. *Adv Energy Mater* 2022, **12**: 2102932.

[33] Ryu KS, Kim KM. Electrochemical performance of chemically synthesized oligo-indole as a positive electrode for lithium rechargeable batteries. *J Appl Electrochem* 2008, **38**: 477–482.

[34] Berkes BZB, Bandarenka AS, Inzelt GR. Electropolymerization: Further Insight into the Formation of Conducting Polyindole Thin Films. *J Phys Chem C* 2015, **119**: 1996–2003.

[35] Chulliyote R, Hareendrakrishnakumar H, Raja M, *et al.* Enhanced cyclability using a polyindole modified cathode material for lithium sulphur batteries. *Sustainable Energy Fuels* 2017, **1**: 1774–1781.

[36] Wang Y, Virkar AV, Zhou XD. On the Thermodynamic Origin of the Formation of Li-Dendrites in an Electrochemical Cell. *J Electrochem Soc* 2021, **168**: 100503.

[37] Yu W, Wang H, Hu J, *et al.* Molecular Sieve Induced Solution Growth of Li_2O_2 in the Li-O_2 Battery with Largely Enhanced Discharge Capacity. *ACS Appl Mater Interfaces* 2018, **10**: 7989–7995.

[38] Plunkett ST, Kondori A, Chung DY, *et al.* A New Cathode Material for a Li–O_2 Battery Based on Lithium Superoxide. *ACS Energy Lett* 2022, **7**: 2619–2626.

[39] Leverick G, Feng S, Acosta P, *et al.* Tunable Redox Mediators for Li-O_2 Batteries Based on Interhalide Complexes. *ACS Appl Mater Interfaces* 2022, **14**: 6689–6701.

[40] Yan A, Xiao X, Zhang Z, *et al.* Mechanistic Understanding of the Solid Product in O_2-Involved Li-CO_2 Batteries. *Battery Energy* 2025, **4**: e70001.

[41] Liu P, Su H, Liu Y, *et al.* LiBr-LiF-Rich Solid–Electrolyte Interface Layer on Lithiophilic 3D Framework for Enhanced Lithium Metal Anode. *Small Struct* 2022, **3**: 2200010.

[42] Wang C, Hao Z, Hu Y, *et al.* Enabling dendrite-free and high-rate lithium anode with a self-standing anionic-MOF separator. *J Mater Chem A* 2023, **11**: 8131–8140.

Just Accepted

[43] Zhang Z, Xiao X, Yan A, *et al.* Breaking the capacity bottleneck of lithium-oxygen batteries through reconceptualizing transport and nucleation kinetics. *Nat Commun* 2024, **15**: 9952.

[44] Chen J, Quattrocchi E, Ciucci F, *et al.* Charging processes in lithium-oxygen batteries unraveled through the lens of the distribution of relaxation times. *Chem* 2023, **9**: 2267–2281.

[45] Zhang S, Dou Y, Xia T, *et al*. Achieving electrocatalytic activity toward oxygen reduction reaction based on Ruddlesden-Popper type cathode catalyst for solid oxide fuel cells. *J Adv Ceram* 2025, **14**: 9221178.

Just Accepted